JOURNAL OF SPACECRAFT AND ROCKETS
Vol. 60, No. 6, November–December 2023

Co-Delivery of a Martian Probe Network

Samuel W. Albert* and Hanspeter Schaub†
University of Colorado Boulder, Boulder, Colorado 80303

https://doi.org/10.2514/1.A35560

Motivated by a need for lower-cost planetary science missions to Mars, this study considers the problem of co-delivering a network of small rough landers to the Martian surface such that the probes are placed on different entry trajectories by a single carrier spacecraft without requiring translational maneuvers between probe deployments. The Small High Impact Energy Landing Device is used as a reference design, and a flight-mechanics analysis is performed to ensure requirements are met under the influence of relevant uncertainties. A linearized targeting method is developed and applied to design probe jettison velocities for a regional probe network. Monte Carlo analysis shows that a regional network approximately 100 km in scale could be passively co-delivered with limited deformation of the network shape despite the influence of relevant uncertainties, and linearized targeting errors are quantified. Nonlinear numerical optimization is applied and enables the design of probe jettisons for co-delivery of larger-scale networks. Additional Monte Carlo analyses quantify the rate at which delivery error increases with network scale.

I. Introduction

ENTRY, descent, and landing (EDL) systems for Mars missions are complex and typically involve multiple mission-critical subsystems that must operate autonomously in harsh conditions [1]. Bringing the risks associated with these subsystems down to acceptable levels is a significant engineering challenge, and this is one reason why, as the size and complexity of payloads to the Martian surface have increased over time, mission costs have also increased [2]. The top priority for Mars surface missions in this decade is Mars Sample Return (MSR), which is a multimission campaign estimated to cost 3.8–4.4 billion U.S. dollars (USD) from formulation through launch and will require significant technology development [3]. It is in this context that a community of planetary scientists and engineers is seeking lower-cost mission concepts and delivery vehicles to enable a sustained program of Mars surface exploration during and after MSR, as outlined in a recent report from the Keck Institute for Space Studies (KISS) [4]. These concepts were further explored in a 2022 workshop, Low-Cost Science Mission Concepts for Mars Exploration [5].

One mission category examined by the KISS study as a potential pathway to reduced cost is networks of small, fixed landers without requirements for surface mobility and with tolerance for relatively high g-loads at landing [4]. These network missions are of growing interest for a variety of investigations, including atmospheric science and seismology [4–8]. In some cases, relevant instruments can be built at small size (5–15 kg) and with high g-load tolerance (1000–2000 Earth g) [9,10]. In general, for these mission concepts, the probes must be delivered to a surface arrangement with roughly the right size and shape, but precision landing is unimportant. Notionally, a probe network would consist of four to eight probes delivered to Mars by a single carrier spacecraft, and networks of regional (tens of kilometers), mid-range (hundreds of kilometers), and global sizes are all potentially of interest. A wide variety of network missions for Mars have been proposed [11–17], but none have come to fruition. In most cases, these missions were cancelled early in development due to high-level budgetary and programmatic issues, which were influenced in part by the failures of the Mars Observer and Mars Polar Lander missions [4]; see appendix A.3 of Ref. [4] for a brief history of Mars network mission concepts. The Mars '96 and Mars Microprobes technical failures are notable exceptions. A significant reduction in the cost and complexity of a Martian probe network could therefore improve the likelihood of selection and successful development of such a mission.

Probe network missions characterized by miniaturized instruments, high g-load tolerance, and the lack of a requirement for precision landing enable the use of small, simplified landing platforms with minimal flight-control requirements. The Small High Impact Energy Landing Device (SHIELD), illustrated in Fig. 1 [20], is a vehicle concept under development at the NASA Jet Propulsion Laboratory (JPL) that would meet these needs [18]. The purpose of SHIELD would be to deliver payloads of about 5 kg to the Martian surface at greatly reduced cost and complexity; the notional cost target for a single SHIELD lander is 50 million USD [18], as compared to a development cost of 371 million USD for the Mars Pathfinder mission [4]. These reductions would be achieved by eliminating EDL subsystems wherever possible, relying entirely on a passive aeroshell-only entry system followed by a hard landing attenuated by crushable material, notionally resulting in landing decelerations on the order of 1000 Earth g [18]. As a point of comparison, the expected landing g-load for the Mars Microprobes, a pair of small probes designed to penetrate the Martian surface upon impact, was 30,000 g [19].

Mission complexity may be further reduced if all of the probes could be co-delivered by a single carrier spacecraft onto their uncontrolled entry trajectories without requiring intervening translational maneuvers between probe deployments. The carrier spacecraft provides necessary resources to the probes during cruise and eliminates the need for attitude control or propulsion subsystems on the probes. The timing, magnitude, and direction of each probe's separation from the carrier spacecraft are aspects of the mission design faced with competing requirements. In the case of late probe separation, the impact of probe jettison execution error is reduced, and less battery life is required for the probe to survive between separation and landing. In contrast, for an early probe separation, the required jettison speed is smaller, and there is more time to estimate and correct any execution error.

Delivery of a passive probe to entry from a carrier spacecraft on a hyperbolic approach trajectory is not inherently a new architecture. The Galileo and Cassini–Huygens missions both successfully delivered probes to entry trajectories before performing orbit insertion [21,22]. The sample return missions of Genesis [23], Stardust [24], Hayabusa [25], and Hayabusa-2 all delivered sample return capsules to Earth entry from a hyperbolic carrier [26], as will the upcoming OSIRIS-REx (Origins, Spectral Interpretation, Resource Identification, Security-Regolith Explorer) and Mars Sample Return (Earth entry system) missions [27,28]. The upcoming DAVINCI (Deep Atmosphere Venus Investigation of Noble gases, Chemistry, and Imaging) mission will also include a passive probe delivered by a carrier spacecraft [29]. What all of these examples have in common, however, is that only a single probe is delivered in each case.

Received 15 September 2022; revision received 23 April 2023; accepted for publication 7 May 2023; published online 28 June 2023.

*Ph.D. Candidate, Ann and H. J. Smead Department of Aerospace Engineering Sciences, 431 UCB, Colorado Center for Astrodynamics Research. Student Member AIAA.

†Professor and Department Chair, Schaden Leadership Chair, Ann and H.J. Smead Department of Aerospace Engineering Sciences, 431 UCB, Colorado Center for Astrodynamics Research. Fellow AIAA.

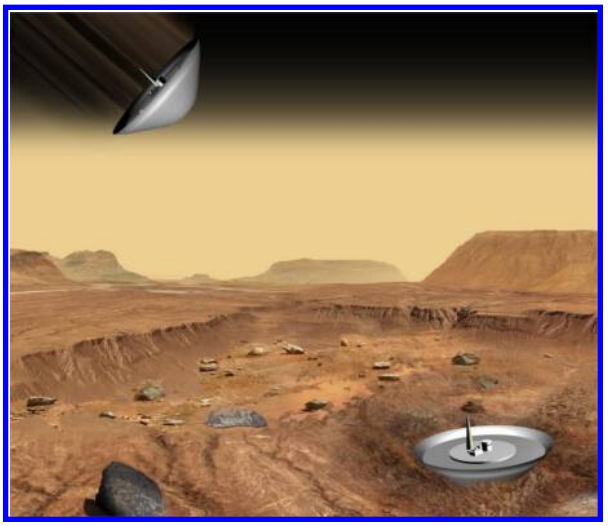

Fig. 1 SHIELD concept image [20].

Recent work for the Aeolus mission concept presents a design that co-delivers 20 probes to a global network on Mars from a single hyperbolic carrier, but it assumes that the carrier maneuvers after each probe deployment [30]; this assumption is typical to previous studies of Mars network missions. A 2013 study demonstrates a unique method of co-delivery wherein two Phoenix-class landers enter the atmosphere together and then separate, one lander with a drag skirt and the other without [31]. This creates a discrete change in the ballistic coefficients for both vehicles and is shown to achieve a 3000 km separation on the surface [31]. However, this method requires separation between two flight vehicles during hypersonic flight, which is a potentially risky event, and assumes a significantly larger landed mass than will be considered in this study. Broadening the scope from planetary probes to include defense applications, missiles armed with multiple independently targetable reentry vehicles are capable of delivering multiple warheads to separate locations from a single carrier vehicle on a suborbital trajectory [32]. Due to limited publicly available information and significant differences in mission scenarios, defense applications are not further considered here.

In terms of planetary entry missions, the Pioneer Venus Multiprobe provides the most relevant example. One large probe and three small probes were delivered from a single spacecraft bus during hyperbolic approach, with the small probes accurately targeted to predetermined entry locations separated by 8800 to 10,400 km [33]. The Multiprobe bus first released the large probe; then, it performed a small maneuver, reoriented, and increased its rate of spin to 48.5 rpm [34]. The three small probes were then released simultaneously, achieving their desired separation due to the tangential velocity provided by the spinning bus [34]. This represents a unique approach to probe co-delivery without intervening maneuvering, and it provides a degree of flight heritage for the concept. However, the Pioneer Venus mission design does not amount to a systematic study of co-delivery trajectory design. Recent work does provide a systematic study of co-delivery trajectories [35], but it considers co-delivery of a probe with an orbiter performing aerocapture rather than multiple probes forming a network.

The purpose of this study is to broadly investigate the probe network co-delivery problem, assuming no intervening translational maneuvers and using SHIELD as an example probe design. Although literature related to specific probe networks does exist, as summarized earlier in this Introduction, this paper provides a more systematic study of the co-delivery problem under a set of assumptions relevant to missions of current-day interest. This work begins by presenting a flight-mechanics analysis for the SHIELD probe, considering event timing, landing accuracy, and the effect of varying entry flight-path angles. The problem of co-delivering probes to form a surface network is then considered: first for regional networks within 100 km of a central point, followed by results for larger-scale networks. A novel linearized targeting method, inspired by B-plane targeting, is introduced for the design of regional networks, and its limitations are quantified. Monte Carlo analyses are performed for both regional and large-scale networks to capture the impact of relevant uncertainties, including probe jettison execution error, on the feasibility of the computed co-delivery trajectories.

II. Models and Assumptions

An assumed design goal in this work is that precision landing is not required, but the network should approximate a desired distribution and location on the surface. Additional assumptions regarding probe co-delivery include the following:

1) Each probe is a ballistic rough lander and is passive, other than drag skirt deployment and heat shield jettison.

2) The probes approach Mars on a single carrier spacecraft on an entry trajectory, the separation events do not change the carrier's trajectory, and no other maneuvers are performed. However, changes in carrier attitude between separation events are allowed.

3) The probes separate from the carrier mechanically.

4) Probe jettisons occur between 0.25 and 20 days before atmospheric entry.

5) The carrier spacecraft has an approach trajectory such that the magnitude of the planet-relative velocity at the atmospheric entry interface altitude of 125 km is 6 km/s.

The approach trajectories in this study are defined by their state at atmospheric entry interface, that is, the position and velocity of the carrier spacecraft at 125 km altitude. This state is defined by the altitude h, longitude θ, latitude ϕ, planet-relative velocity V, flight-path angle γ, and heading angle ψ; the flight-path angle is the angle between the velocity vector and the local horizon, and the heading angle is the angle between the horizontal projection of the velocity vector and a due-north vector in that same plane (e.g., a 90 deg heading angle is due east). Figure 2 provides a visualization for these definitions, where the $\hat{\imath}$ basis vectors form a planet-fixed frame, $\hat{\boldsymbol{e}}_1$ is aligned with the position vector of the spacecraft, and $\hat{\boldsymbol{s}}_3$ is aligned with the planet-relative velocity vector. The central landing site is then the point on the surface where a SHIELD probe would nominally land after continuing on this trajectory. Two things should be noted about this convention. First, because of the probe jettison velocities, each probe will actually enter the atmosphere with different states, potentially resulting in significantly different entry flight-path angle and entry velocity values. Second, the carrier spacecraft would not itself be a SHIELD probe and could perform a divert maneuver or intentionally burn up in the atmosphere; the carrier's entry state and central landing site are simply convenient ways to define the approach trajectory and a reference point on the surface, respectively.

Separation events are assumed to impart an impulsive change in velocity to the probe, where the jettison velocity $\boldsymbol{V}_j$ is defined as the velocity of the probe relative to the carrier the moment after separation, and the jettison speed is defined as the magnitude $V_j = |\boldsymbol{V}_j|$. This notation is used to distinguish from impulsive $\Delta\boldsymbol{V}$ because, although they are theoretically equivalent events, this study assumes jettisons occur mechanically (e.g., a spring jettison) rather than propulsively.

Although mostly passive, SHIELD does go through three different configurations from atmospheric interface to surface. First, in its *entry* configuration, SHIELD is entirely within its protected aeroshell, and this configuration is maintained through the hypersonic and high-heating portion of the flight. Next, SHIELD enters the *descent* configuration soon after beginning subsonic flight by deploying a drag skirt, the purpose of which is to reduce the terminal velocity of the vehicle. Shortly thereafter, the *landing* configuration is initiated with the jettison of the heat shield. SHIELD is assumed to fly at a trim zero angle of attack and has an axisymmetric shape with balanced center of mass, resulting in a lift-to-drag ratio of $L/D = 0$. The drag properties of SHIELD are linearly interpolated based on Mach number from tabular data provided by the JPL SHIELD team, resulting in ballistic coefficients ranging from about 20 $\mathrm{kg \cdot m^{-2}}$ in the entry configuration down to around 5 $\mathrm{kg \cdot m^{-2}}$ in the landing configuration. Ballistic coefficient describes the ratio of inertial to aerodynamic forces and is defined as $\beta = m/(C_D A)$, where m is the

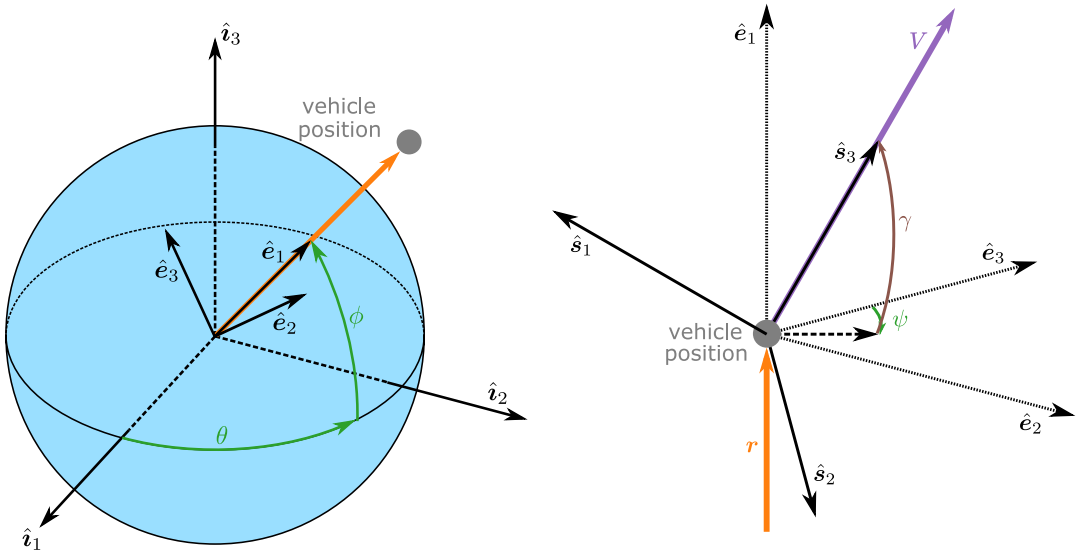

a) Planet-fixed and position frames **b) Position and velocity frames**

Fig. 2 Frame definitions.

Table 1 Monte Carlo analysis input dispersions

Parameter	Dispersion
Entry interface flight-path angle γ_0	$3\sigma = 0.2$ deg
Entry interface velocity magnitude V_0	$3\sigma = 2$ m/s
Atmospheric density ρ	MarsGRAM 2010
Probe ballistic coefficient β	$\pm 5\%$
Jettison speed V_j	$\pm 10\%$

mass, C_D is the drag coefficient, and A is the aerodynamic reference area. SHIELD is assumed to have a nose radius of $R_n = 0.85$ m.

Table 1 summarizes the relevant uncertainties applied throughout this study. Uncertainty in the approach trajectory of the carrier spacecraft is modeled by dispersing the state at atmospheric entry interface for each trial and then backpropagating the dispersed state to the time of the first jettison. Interplanetary navigation to Mars has advanced to the extent that its contribution to the landing error is small when compared to the impacts of atmospheric variability and aerodynamic modeling errors,[‡] even for unguided entry. For example, the navigation-only errors for the Mars Exploration Rovers (MERs) were 3.3 km for *Spirit* and 9.7 km for *Opportunity* [36]. Furthermore, the large majority of landing error is in the downrange direction; the final landing ellipses predicted for the MERs due to all error sources had crossrange components below 5 km, as compared to approximately 60 km in downrange [36], indicating high accuracy in heading angle at entry. The driving requirement for approach navigation is precise targeting of the entry interface flight-path angle [36–38], γ_0, because even small variations can have a significant effect on the altitude–velocity entry profile [39]. The velocity magnitude at entry interface, V_0, is also relevant because of its impact on key quantities like peak heat flux and peak deceleration. These two entry state components are dispersed independently according to Gaussian distributions centered at the nominal value and with some standard deviation σ. For this study, the 3σ value for γ_0 is set equal to the requirement on the delivery error for the Mars Science Laboratory (MSL), and the 3σ value for V_0 is set equal to the required knowledge accuracy at EDL guidance system initialization for MSL [37]. In contrast, minor errors in entry position and heading angle have very little impact on the altitude–velocity profiles of the probes, and thus primarily contribute a small center error for the network without adding significant shape error. Recall that it is an assumption of this study that small errors in network center are unimportant when compared to the distribution of the probes. Therefore, the longitude, latitude, and heading angle at entry interface are not dispersed in this study.

Variability of atmospheric density is modeled by using random profiles of the density vs altitude that are generated using the 2010 version of the Mars Global Reference Atmospheric Model (MarsGRAM 2010) [40]. For a given trial, the dispersions on the atmosphere, γ_0, and V_0 are applied once, such that all probes experience the same atmosphere and carrier spacecraft trajectory.

The ballistic coefficient of each probe is dispersed along a uniform distribution with bounds at $\pm 5\%$ of the nominal value. This value is representative of the confidence level provided by computational fluid dynamics and ballistic range testing, and it is chosen based on previous studies [35,41]. The lift-to-drag ratio always remains at its nominal value of zero, assuming that axisymmetric spin removes the effect of any small, unintended lift force. Finally, the magnitude of the jettison event is dispersed along a uniform distribution with bounds at $\pm 10\%$ of the nominal value under the assumption that a separation mechanism could be designed to within this uncertainty level; through discussions with mission engineers, this was judged to be a conservative assumption. The directions of the jettison velocities are assumed to be nominal for the purposes of this study. These two dispersions are applied independently to each probe for each trial. Finally, note that although the carrier entry longitude, latitude, and heading angle are not dispersed, individual probes may have off-nominal values of these parameters due to jettison speed dispersions, and these effects are accounted for.

Trajectories are computed via numerical propagation of the three-degree-of-freedom equations of motion for a rotating ellipsoidal planet using explicit Runge–Kutta integration of order 4(5) with relative and absolute tolerances equal to 1×10^{-11} [39]. Mars is assumed to have a gravitational parameter of $\mu = 4.305 \times 10^4$ km^3 s^{-2}, an equatorial radius of $R = 3397.2$ km, an oblateness spherical harmonic coefficient of $J_2 = 0.001964$, and a planetary rotation period of $T = 1.02595675$ days [42]. The speed of sound for the Martian atmosphere, which is used to compute Mach number, is interpolated from a nominal tabular model [43]. Heat flux is modeled by computing convective heat flux $\dot{q}$ at the stagnation point assuming a fully catalytic surface using the Sutton–Graves expression shown in Eq. (1) [44], where ρ is density and a value of the heating coefficient $k = 1.904 \times 10^{-4}$ kg$^{0.5}$/m is used based on nominal atmospheric composition at Mars [45]:

$$\dot{q} = k\sqrt{\frac{\rho}{R_n}}V^3 \tag{1}$$

[‡]Note, however, that this statement assumes significant Deep Space Network coverage during approach, which may be a limiting factor for small missions.

Finally, sensed deceleration (or g-load) is computed as $g = \sqrt{L^2 + D^2}/g_0$, where L and D are the accelerations due to the lift and drag, respectively, and g_0 is the standard acceleration due to gravity at the Earth's surface.

III. SHIELD Flight Mechanics

Before investigating co-delivery of networks, a flight-mechanics analysis is presented for the atmospheric flight of a single SHIELD probe in order to determine feasible nominal values for drag skirt deployment and heat shield jettison. This analysis also assesses the robustness to uncertainty of time-triggered configuration changes and the possibility of using drag skirt deployment timing as a method of control. The analysis is performed at several representative entry interface flight-path angles: −12, −18, and −24 deg.

First, EDL event timing is considered. Drag skirt deployment and heat shield jettison are constrained by three parameters: the maximum Mach number at drag skirt deployment, the maximum impact velocity, and the minimum time between deployment and jettison. The assumed values[§] for these requirements are summarized in Table 2. The combined results of these parameters define an acceptable range for the timing of each event for any entry trajectory, and the nominal event times can then be selected from within this range. The resulting bounds on event timing were computed for $\gamma_0 = -18$ deg, and they were found to be 105.7 s after entry (denoted E+105.7 s) for earliest deployment and E+170.9 s for latest jettison, where in this context entry is defined as the point at which sensed deceleration first exceeds 1 Earth g. Nominal event times of E+140 s and E+150 s were then selected on the basis of being well within this acceptable range, and the resulting trajectory is shown in Fig. 3. A similar analysis was performed for the other values of γ_0, with the results summarized in Table 3.

EDL events are often triggered by processed sensor data, such as commanding parachute deployment using either a velocity trigger or range trigger [46]. For SHIELD, however, the goal of eliminating subsystems wherever possible motivates the following question: Would a simple onboard timer be sufficient to trigger drag skirt deployment and heat shield jettison without violating the assumed requirements when relevant uncertainties are applied? If so, this could simplify EDL for SHIELD even further.

A 1000-trial Monte Carlo analysis is performed at each of the γ_0 values of interest to capture the impact of relevant uncertainties on SHIELD flight mechanics. In each trial, drag skirt deployment and heat shield jettison are triggered once the nominal time after entry is reached, but the conditions at those points along the trajectory vary due to the input dispersions. Figure 4 shows the resulting Mach numbers at deployment; as can be seen from the histogram, none of the cases for any of the γ_0 values exceeded the 0.9 maximum. The requirement on impact velocity was also met, with the maximum value for any of the 3000 total trials being 45.9 m/s; in fact, the impact velocity varied so little that the histograms become unhelpful visualizations, and are thus not shown. This is because the probes always proceeded through the EDL stages on time to reach terminal velocity, which only varied slightly. Because the time between deployment and jettison was enforced by the timer itself, a simple timer was therefore sufficient to trigger EDL events while meeting the requirements for the assumed uncertainties. This result is largely because the acceptable timing range is relatively wide.

Another relevant constraint, peak heat flux, is reported in Fig. 5a. As expected, steeper γ_0 values result in higher heating because deceleration occurs more rapidly. No requirement on peak heat flux is assumed for SHIELD in this study, but these values are well within the capabilities of modern thermal protection systems such as SLA-561V, which has flight heritage for Mars entry missions and has demonstrated good performance at heat fluxes up to 240 W/cm^2 [47]. Additionally, histograms of landing error are shown in Fig. 5b, where error is defined as the distance between the nominal and actual landing sites. Note that there is a major decrease in landing error as the entry flight-path angle gets steeper from −12 to −18 deg; although there is a further decrease for $\gamma_0 = -24$ deg, the returns diminish after some point. Table 4 summarizes the results of these Monte Carlo analyses, where σ is the standard deviation.

Finally, this study also examines the possibility of using the drag skirt deployment and heat shield jettison as methods of range control.

[§]This information is based on discussions with the SHIELD team at JPL.

Table 2 Summary of SHIELD EDL requirements

Parameter	Requirement
Mach number at drag skirt deployment	≤ 0.9
Time between drag skirt deployment and heat shield jettison	≥ 4 s
Impact velocity	≤ 50 m/s

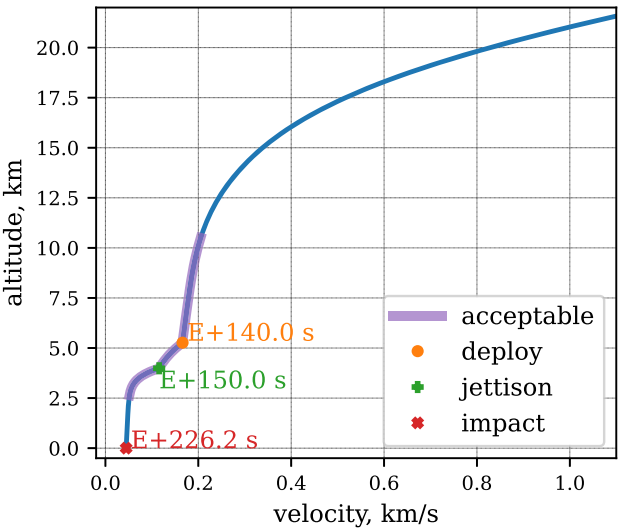

Fig. 3 Nominal trajectory, with event timing annotated, for a SHIELD entry at −18 deg.

Table 3 EDL event timing, in terms of seconds after entry

γ_0	Earliest deployment	Latest jettison	Nominal deployment	Nominal jettison
−12 deg	193.9 s	258.2 s	225 s	235 s
−18 deg	105.7 s	170.9 s	140 s	150 s
−24 deg	76.9 s	132.8 s	105 s	115 s

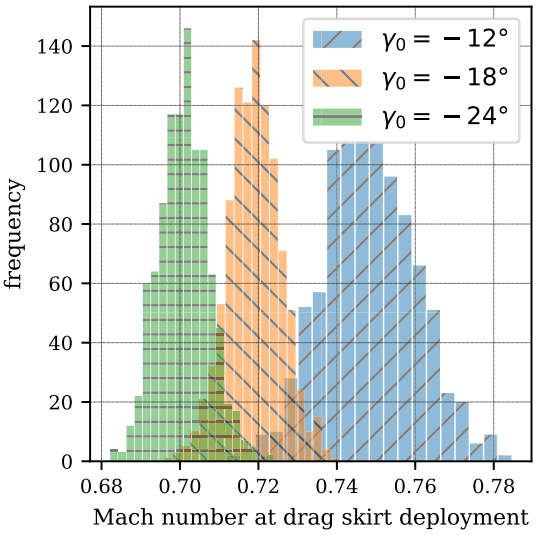

Fig. 4 Monte Carlo results for Mach number at drag skirt deployment at varying γ_0 values.

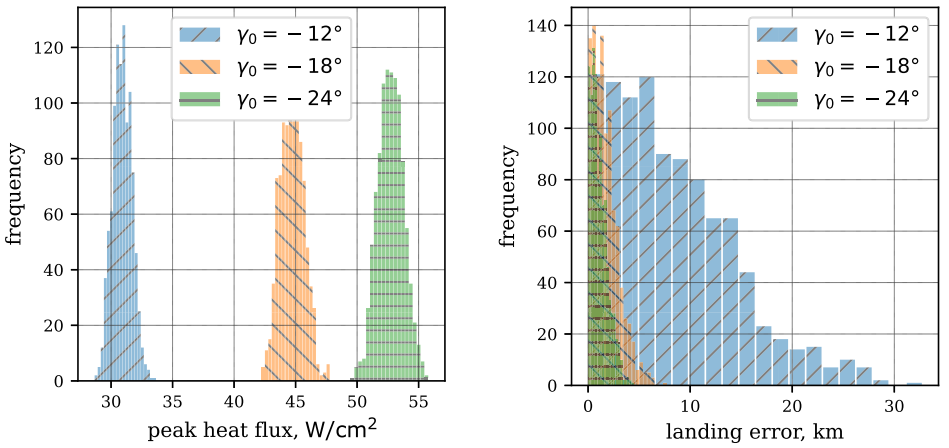

a) Peak heat flux **b) Landing error**

Fig. 5 Monte Carlo results at varying γ_0 values.

Table 4 Summary of Monte Carlo results for EDL of a single SHIELD probe

	Mach at deployment		Impact velocity, m/s		Peak heat flux, W/cm^2		Landing error, km	
γ_0	Mean	σ	Mean	σ	Mean	σ	Mean	σ
−12 deg	0.748	0.0115	44.6	0.801	30.9	0.777	8.29	6.06
−18 deg	0.719	0.00672	44.7	0.792	44.7	0.962	1.70	1.27
−24 deg	0.701	0.00636	44.6	0.783	52.7	1.04	1.12	0.829

By carefully timing these events based on the difference between the nominal and estimated states for the current time, the vehicle could in theory control its in-plane terminal range during entry. In practice, however, the requirement that the drag skirt deploy in subsonic conditions severely limits the total achievable control authority, to the extent that this approach has little or no merit for this application. This is because, by the time the vehicle reaches subsonic speeds, it has already dissipated almost all of its energy and is at a low altitude (about 10 km in this case), leaving little time or energy for the change in ballistic coefficient to significantly impact the landing site. Specifically, for two trajectories at $\gamma_0 = -18$ deg, one with the earliest permissible deployment and jettison times, and the other with the latest permissible times, the two trajectories land only about 3 km apart. This represents the maximum possible control authority yielded by this method; because this is well below the expected landing site dispersions, the approach is discarded as a method of flight control. If the drag skirt could be deployed at supersonic or hypersonic speeds, the control authority would increase substantially and this method would merit reexamination. Indeed, jettison of a drag skirt during hypersonic flight has been shown in the literature to be an effective method of range control for entry at Mars [48,49]. However, the drag skirt for the current SHIELD concept would not structurally or thermally withstand such conditions (see footnote §).

IV. Regional Probe Networks

This section investigates probe jettison velocity design and performs uncertainty quantification for regional networks, which are loosely defined as having all probes within 100 km of the central landing site. Because the changes in trajectory to achieve these separations are relatively small, the relationship between separation time and separation distance, as well as that between jettison speed and separation distance, is roughly linear [50]. A linearized numerical targeting method, developed by the authors and first presented in Ref. [50], is therefore developed and employed to design probe jettisons for a reference network. These trajectories are then subjected to relevant uncertainties to quantify the impact of these dispersions on probe landing locations.

A. Linearized Targeting Method

The linearized targeting method for regional networks is summarized as follows: Assume $\boldsymbol{x}_{\theta\phi} = [\theta, \phi]^T$ to be the landing site coordinates and $\boldsymbol{V} = \boldsymbol{V}(t)$ to be the velocity of the probe at some time before landing. Apply a Taylor series expansion to $\boldsymbol{x}_{\theta\phi}$ about the trajectory of the carrier spacecraft, $\boldsymbol{x}^*_{\theta\phi}$, as a function of velocity, and then neglect terms of second order or higher:

$$\boldsymbol{x}_{\theta\phi} = \boldsymbol{x}^*_{\theta\phi} + \left.\frac{\partial \boldsymbol{x}_{\theta\phi}}{\partial \boldsymbol{V}}\right|_* (\boldsymbol{V} - \boldsymbol{V}^*) + \text{H.O.T.s} \tag{2}$$

$$\Delta\boldsymbol{x}_{\theta\phi} \approx \left.\frac{\partial \boldsymbol{x}_{\theta\phi}}{\partial \boldsymbol{V}}\right|_* \boldsymbol{V}_j = [\boldsymbol{J}]\boldsymbol{V}_j \tag{3}$$

$$[\boldsymbol{J}] = \begin{bmatrix} \frac{\partial\theta}{\partial V_x} & \frac{\partial\theta}{\partial V_y} & \frac{\partial\theta}{\partial V_z} \\ \frac{\partial\phi}{\partial V_x} & \frac{\partial\phi}{\partial V_y} & \frac{\partial\phi}{\partial V_z} \end{bmatrix}_* \tag{4}$$

where the jettison velocity is the velocity of the probe minus the velocity of the carrier spacecraft at the moment after jettison, $\boldsymbol{V}_j = \boldsymbol{V} - \boldsymbol{V}^*$. The Jacobian matrix $[\boldsymbol{J}]$ can then be evaluated for any value of the jettison time to represent the sensitivity of the landing site coordinates to the velocity at that time. By inverting the Jacobian, the $\boldsymbol{V}_j$ vector required to achieve a desired change in the landing location, $\Delta\boldsymbol{x}_{\theta\phi}$, can be linearly approximated. Because the Jacobian in this case is not square, the least-norm solution is selected to minimize the V_j magnitude:

$$\boldsymbol{V}_j = [\boldsymbol{J}]^T([\boldsymbol{J}][\boldsymbol{J}]^T)^{-1}\Delta\boldsymbol{x}_{\theta\phi} \tag{5}$$

For the purpose of this study, $[\boldsymbol{J}]$ is numerically approximated using first-order forward finite differencing; Eq. (6) gives an example for the first element of the matrix:

$$\frac{\partial\theta}{\partial V_x} = \frac{\theta_p - \theta^*}{\Delta V_x} \tag{6}$$

where ΔV_x is a small velocity perturbation in the x-axis direction and θ_p is the landing site longitude that results from applying a jettison velocity of $[\Delta V_x, 0, 0]^T$ and then propagating to surface impact. In this study, a perturbation value of $\Delta V_x = \Delta V_y = \Delta V_z = 1 \times 10^{-4}$ m · s^{-1} was selected based on trial and error. Numerically computing the Jacobian $[\boldsymbol{J}]$ according to Eqs. (4) and (6) allows one to linearly approximate the jettison velocity vector $\boldsymbol{V}_j$ required to achieve a shift in longitude and latitude equal to $\Delta\boldsymbol{x}_{\theta\phi} = [\Delta\theta, \Delta\phi]^T$ for a given separation time. To consider a different jettison time, the Jacobian is simply reevaluated by applying perturbations at that time.

B. Reference Network Design

This linearized targeting method is employed to design probe jettisons for a regional network. As a motivating example, the reference science mission is a seismology network deployed to Cerberus Fossae, a region of known seismicity on Mars [51,52]. A regional network in such an area can obtain useful geophysical measurements using significantly lower-sensitivity seismometers than a global network would require by relying on its proximity to seismic events, thereby bringing the required payload mass down to the range of 2–3 kg per lander[¶] [53]. Shock-tolerant seismology payloads have been developed that can survive 15,000 g at impact [54], and the precision landing of probes is significantly less important than achieving a network geometry that permits observability.

To target Cerberus Fossae, the central state at atmospheric entry interface is defined to have a longitude of 150° East, a latitude of 7.25° North, a flight-path angle of $\gamma_0 = -12$ deg, and a heading angle of 80 deg (slightly northward of due east). The network consists of three pairs of probes such that each pair is targeted with equal and opposite jettison velocities $\pm\boldsymbol{V}_j$, resulting in a symmetrical network of six probes. The nominal configuration is shown to scale in Fig. 6.[**] Note that the distance corresponding to the angular separation, shown on the top and right axes of Fig. 6, is computed as the great-circle distance according to Eq. (10) and assumes a spherical planetary surface. Because Mars is not perfectly spherical, this distance differs from the true distance along the surface and should be treated as approximate for large separations; specifically, for separation angles larger than 15 deg, the difference could exceed 5 km.

The directions of the probe jettison velocities are not constrained to be equal, and thus changes in attitude may be required between probe jettisons. Because the separations are assumed to occur mechanically, designing for a uniform jettison speed is likely more desirable than an outright minimization of jettison speed. To deploy the network using a single jettison speed for all three separations, targeting is performed along a range of separation times to provide trends of the required V_j; these results are shown in Fig. 7. As would be expected, required jettison speed increases dramatically as the time between separation and entry approaches zero. A jettison speed of 10 cm · s^{-1} is selected as a relatively low value that intersects all three curves between 0.5 and five days before entry; note that iterating between these results and the design of the network allows for flexibility in the selection of the nominal jettison speed. A root solver is used to compute the precise jettison time for each probe that targets the desired landing location and results in a jettison speed equal to the desired value, with the approximate intersections of the curves with the dashed line in Fig. 7 providing good initial guesses for the solver. Specifically, Brent's method [††] is applied to within numerical precision with a maximum of 10 iterations [55,56]. The resulting separation times are 0.7613, 1.6529, and 3.1697 days before entry.

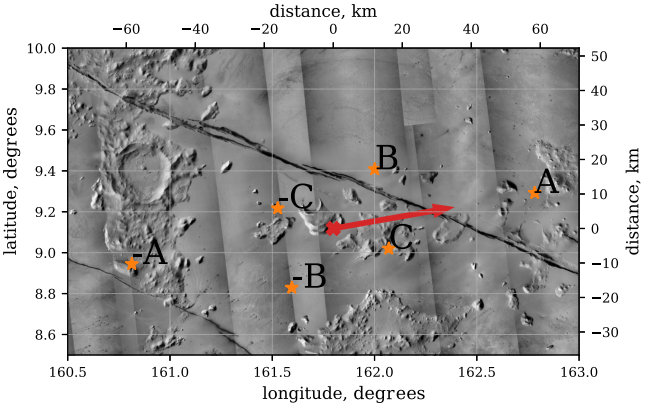

Fig. 6 Nominal landing locations for example network, with downrange direction shown by red arrow and central point shown by red X.

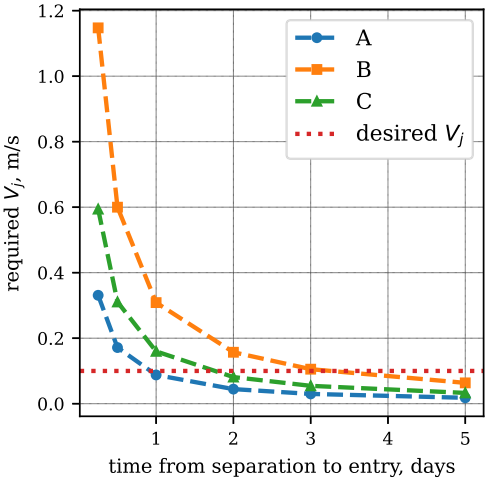

Fig. 7 Required V_j vs. separation time for the three chosen nominal landing sites.

C. Error Parameters

The assumed mission goal is to deploy a network in approximately the correct geometry and location rather than to precisely target each probe. Thus, the separate statistics of landing error for each probe do not directly relate to the performance requirements. To better characterize the network delivery performance, two error parameters are defined: center error ε_c and shape error ε_s. Center error describes the off-nominal location of the center of the network, and shape error describes the off-nominal distribution of probes around that center. Define the center error for any given trial as follows:

$$\varepsilon_c = \sqrt{(\bar{\theta}^* - \bar{\theta})^2 + (\bar{\phi}^* - \bar{\phi})^2} \tag{7}$$

where $\bar{\theta}^*$ and $\bar{\phi}^*$ are the average longitude and latitude, respectively, across all probe locations for the *nominal* network design, and $\bar{\theta}$ and $\bar{\phi}$ are the average longitude and latitude of the actual probe landing sites. This error is computed in radians and can be converted to distance by multiplying by the planet's radius. To calculate the shape error, compute the great-circle distance between every unique pair of landing sites, yielding $d = N(N-1)/2$ distances for N probes, and label these values as δ_i^* and δ_i for the nominal and actual landing sites, respectively. The shape error is then defined as the root sum squared of the differences between the nominal distance and the actual distance for each unique pair of landing sites divided by the total number of probes N:

[¶]This assumption of the total payload mass for a seismometer of the required sensitivity is based on the short-period instrument onboard the InSight lander and private communications with Mark Panning in December 2021.

[**]The surface image in Fig. 6 is a mosaic created from data acquired from the context camera onboard NASA's Mars Reconnaissance Orbiter and was generated using MarsTrek at trek.nasa.gov/mars [retrieved 15 September 2022].

[††]scipy.optimize.brentq, https://docs.scipy.org/doc/scipy/reference/generated/scipy.optimize.brentq.html.

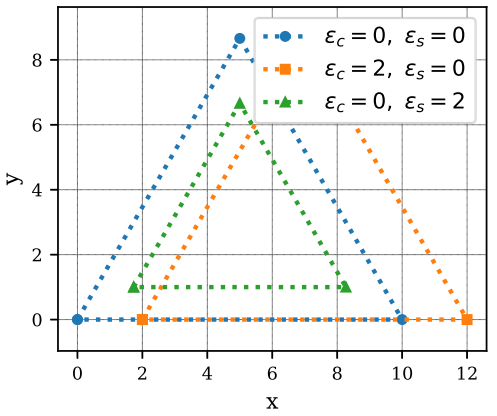

Fig. 8 Three example networks, illustrating center error ε_c vs. shape error ε_s.

$$\varepsilon_s = \frac{\sqrt{(\delta_1^* - \delta_1)^2 + \cdots + (\delta_d^* - \delta_d)^2}}{N}, \qquad d = \frac{N(N-1)}{2} \tag{8}$$

A more intuitive representation of these parameters is provided by Fig. 8, which shows a generic nominal network in blue circles. The orange squares have the correct network shape, but all points are shifted to the right, resulting in $\varepsilon_c = 2$ and $\varepsilon_s = 0$. The green triangles are centered correctly, but the entire geometry has been reduced in size, resulting in $\varepsilon_c = 0$ and $\varepsilon_s = 2$.

D. Dispersion Analysis

The results of applying relevant uncertainties to this reference scenario in a 1000-trial Monte Carlo analysis are shown in Fig. 9. As expected based on intuition and the earlier flight-mechanics analysis, the probes experience large dispersions in landing sites, primarily in the downrange direction. However, it turns out that these dispersions are highly correlated between probes for any given trial because all dispersions except the jettison speed and ballistic coefficient apply to the trial as a whole and affect all of the probes in more or less the same way. For this scenario, dispersions on the jettison speed have relatively little effect because the nominal speeds are low enough to be within the regime of roughly linear sensitivity for these trajectories. As a result of all this, the network shifts back and forth in the downrange but its shape deforms relatively little. This is reflected in the statistics of the center and shape error, which is summarized in

Table 5 Statistics of error parameters

Parameter	Mean	3σ
Center error ε_c, km	7.391	16.573
Shape error ε_s, km	3.335	3.555
min. separation, km	22.029	2.569
max. separation, km	119.370	22.554
avg. separation, km	52.491	8.126

Table 5: the minimum, maximum, and average distances between every unique pair of landing sites are computed for each trial; and the statistics of these values are shown in Table 5. The landing locations for the trial with the largest shape error are shown in the red pentagons in Fig. 9. It can be seen by inspection that the network shape in this trial is qualitatively similar to the nominal shape, but with an offset in the positive downrange direction. The key takeaway is that, for the example regional network considered here, the probes can be delivered to roughly the desired arrangement on the surface despite large dispersions for each individual probe, so long as roughly ±25 km downrange shifts of the entire network can be tolerated.

E. Limits of Linearization

The linear approach to targeting applied in this section is a good approximation only within some local region of the reference trajectory, that is, near the approach trajectory of the carrier spacecraft leading to the central entry point. Thus, it is important to quantify the limits of applicability for the linearization. To do so, the linearized targeting method is applied to compute a probe jettison velocity, targeting progressively greater offsets from the central point in both the downrange and crossrange directions, as well as assuming separation one day before entry along the approach trajectory defined in Sec. IV.B. A trajectory is then simulated for each probe jettison, and the great-circle distance between the achieved landing site and the targeted offset defines the error. Figure 10 shows this error along with the jettison speed computed by the linearized targeting. The x-axis shows the targeted offset in terms of the separation distance (top), which is essentially the great-circle distance, and the corresponding separation angle (bottom), e.g.,

$$\text{separation distance} = \text{separation angle} \times \text{planetary radius}$$

From these results, it is clear that after about 100 km of desired separation distance, the approximation error due to linearization

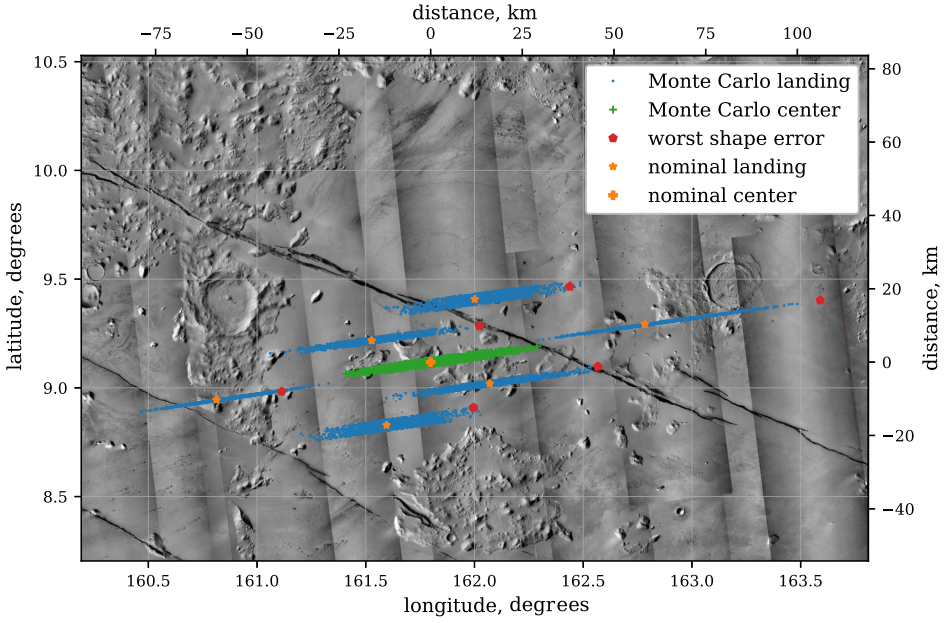

Fig. 9 Nominal and random trial landing locations shown against to-scale Martian surface.

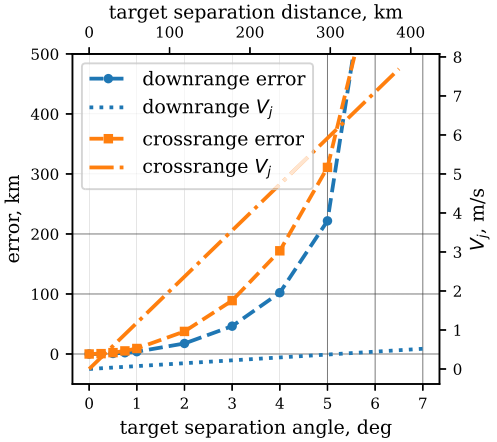

Fig. 10 Error and required V_j for linearized targeting for varying downrange and crossrange spacing. After the desired change in angle exceeds 6.5 deg, both cases begin to miss the planet entirely.

begins to increase rapidly. By about 300 km of desired separation, the targeting error is of similar magnitude to the desired separation; thus, under these assumptions, the linearized targeting method has no utility beyond this point.

V. Large-Scale Probe Networks

The linearization method presented in the previous section fails for networks that extend beyond about 100 km from the central point, requiring a different approach. In this section, a numerical nonlinear optimization tool is applied to design probe jettisons for large-scale networks of co-delivered probes, and a similar uncertainty quantification analysis is performed.

A. Nonlinear Optimization Procedure

The quasi-Newton method of Broyden, Fletcher, Goldfarb, and Shanno (BFGS[‡‡]) is used to numerically perform unconstrained optimization of a scalar cost function by iteratively approximating the Hessian matrix [55,57], where the design variables are the three components of the jettison velocity. Each trajectory is propagated until either reaching the surface or reaching a final time, where the final time is defined to be much later than the nominal time at the target. The cost function being minimized is nominally the great-circle distance d along the surface between the target and achieved landing locations, assuming a spherical planet. In certain cases, this can result in erroneous convergence to a flyby or skip-out trajectory that never reaches the surface but is at the correct latitude and longitude at the final time. To account for this possibility, the altitude of the spacecraft at the final time is added to the cost function. Equation (9) gives the resulting cost function, where (θ_t, ϕ_t) and (θ_f, ϕ_f) are the target and achieved landing coordinates, respectively, and r_f is the radial distance of the spacecraft at the final time. The tolerance is 1 km, meaning that the computed probe jettison velocity delivers the probe to within 1 km, or approximately 0.0169 deg, of the target landing location.

$$J(\boldsymbol{r}_f, \boldsymbol{v}_f) = d + r_f - R \tag{9}$$

$$d = R\cos^{-1}(\sin\phi_f \sin\phi_t + \cos\phi_f \cos\phi_t \cos(|\theta_t - \theta_f|)) \tag{10}$$

B. Targeting Results

For these scenarios, a generic entry interface state of 0° longitude, 0° latitude, and a 90 deg (due east) heading angle is assumed, such that the downrange and cross range are directed east–west and north–south, respectively. Downrange and crossrange separations are treated separately in this analysis based on the significant difference in the required jettison speeds, as shown in Fig. 10; this is also intuitive from orbital mechanics, wherein changing the plane of motion in general takes greater effort than changes of similar magnitude within the plane of motion.

Figure 11 explores the relationships between desired separation, required jettison speed, and entry flight-path angle for both downrange and crossrange separations, with separation performed three days before entry. As expected, larger separations tend to require larger jettison speeds. This relationship takes a roughly linear form for crossrange separations, as shown in Fig. 11b, despite the breakdown of the linearization method based on finite differencing from small perturbations. Furthermore, γ_0 of the approach trajectory has very little effect on the required jettison speed. In sharp contrast, the jettison speed required for downrange separations asymptotically approaches a fixed value beyond 30 deg of separation, and is strongly affected by the approach trajectory γ_0. Note that the y-axis of Fig. 11a is normalized with respect to the required jettison speed of the largest separation, highlighting the similarity in shape between the different γ_0 cases despite their offset values, whereas Fig. 11b shows non-normalized speeds.

The reason for the plateau in jettison speed shown in Fig. 11a is that downrange separations larger than 15 deg are achieved via either long coast phases in the atmosphere or skip-out trajectories, in which the vehicle exits the atmosphere on a suborbital arc and then reenters farther downrange. This can be seen in Fig. 12, which shows trajectories targeting downrange separation for the $\gamma_0 = -18$ deg case, where Fig. 12a plots planet-relative motion in the altitude vs downrange plane and Fig. 12b shows trajectories in the planet-centered inertial frame. The three cases with the smallest separations can be seen to follow similarly shaped trajectories down to the surface, separated due to offsets in their exoatmospheric trajectories and incremental changes in their entry interface states. The rest of the trajectories, however, enter the atmosphere on nearly the same trajectory and then achieve separation during atmospheric flight, with each subsequent trajectory coasting for longer in the atmosphere until skip-out trajectories are eventually realized. Sensitivity of the landing separation with respect to the state at entry interface increases dramatically for these long coast or skip-out trajectories. The use of increasingly long atmospheric flight phases to achieve downrange separation is also the reason that the entry flight-path angle of the approach trajectory significantly impacts the required jettison speed. In contrast, crossrange separation is achieved primarily by modifying the exoatmospheric trajectory, and is thus insensitive to the approach trajectory γ_0.

All of the large-scale network results thus far assume a separation time of three days before entry. Therefore, it is instructive to consider the relationship between separation time and required jettison speed, particularly for crossrange separation since the required speeds are larger in those cases. To this end, Fig. 13a compares required jettison speed vs desired separation for separation events three and 18 days before entry. The required speeds for 18 days before entry are not only lower but also increase at a slower rate as compared to separation three days beforehand. Figure 13b shows how required jettison speed changes with varying separation timing for a 5 deg crossrange separation; one can imagine this as representing the continuum between the leftmost points of the two lines in Fig. 13a. The required jettison speed decreases monotonically and nonlinearly as the time between separation and entry increases, as is the case for regional networks as shown in Fig. 7.

C. Dispersion Analysis

The preceding results demonstrate the ability to use nonlinear numerical optimization to design probe jettisons to co-deliver large-scale probe networks. To understand the practicality of these trajectories, however, the impact of relevant uncertainties must be considered. A 1000-trial Monte Carlo analysis is performed for this purpose, assuming $\gamma_0 = -18$ deg and using the same input dispersions as in the previous section. In this case, eight total probes are considered. Four probes target downrange separations of 5, 10, 15, and 30 deg, and separate from the carrier three days before entry. The other four probes target crossrange separations of the same magnitudes and separate from

[‡‡]scipy.optimize.BFGS, https://docs.scipy.org/doc/scipy/reference/generated/scipy.optimize.BFGS.html.

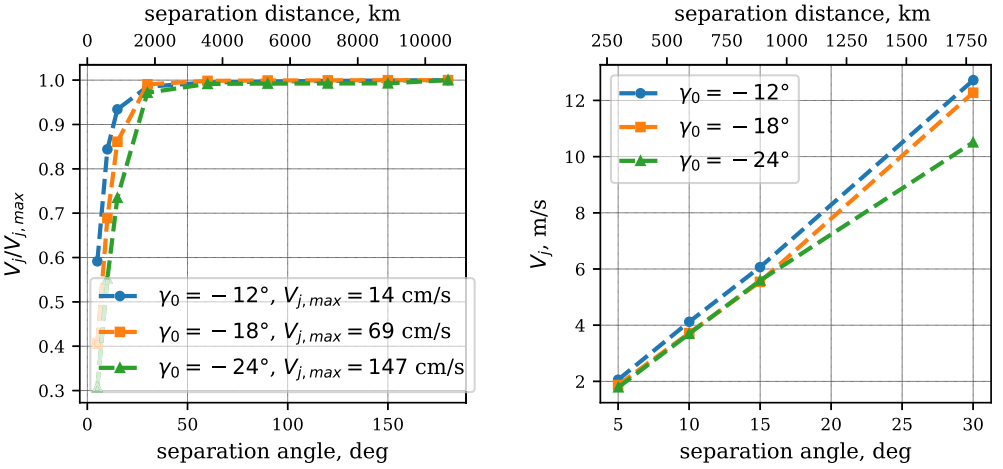

a) Downrange separation **b) Crossrange separation**

Fig. 11 Required jettison speed vs. desired landing separation, for separation 3 days before entry and varying γ_0 values.

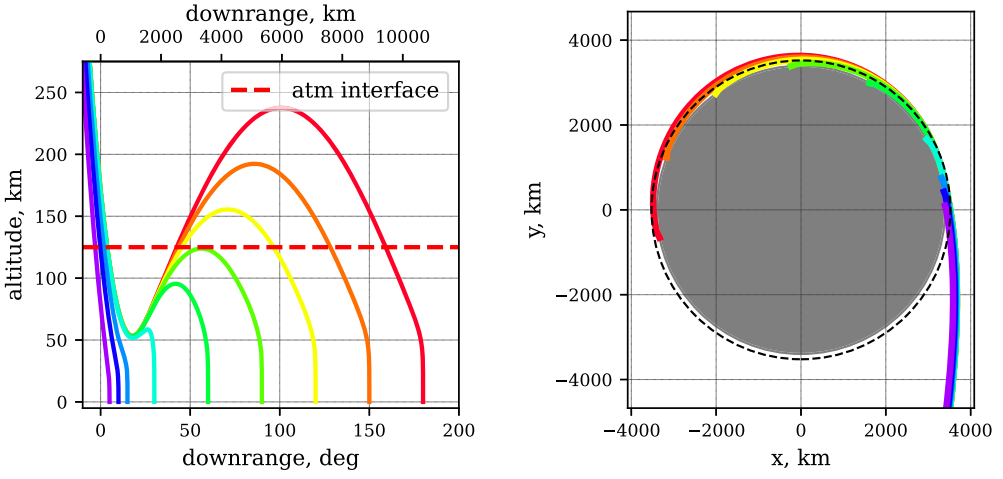

a) Altitude vs downrange **b) Viewed down from North Pole, inertial**

Fig. 12 Probe trajectories for downrange separations ranging from 5 deg (purple) to 180 deg (red).

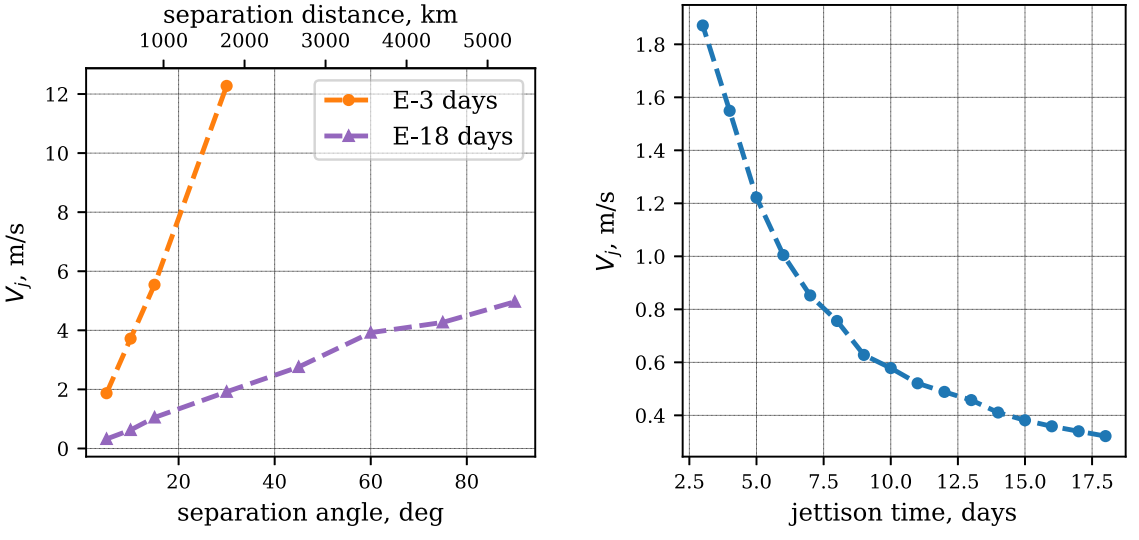

a) Varying crossrange separation **b) 5 deg crossrange separation**

Fig. 13 Comparisons of required jettison speed at varying separation times, for $\gamma_0 = -18$ deg.

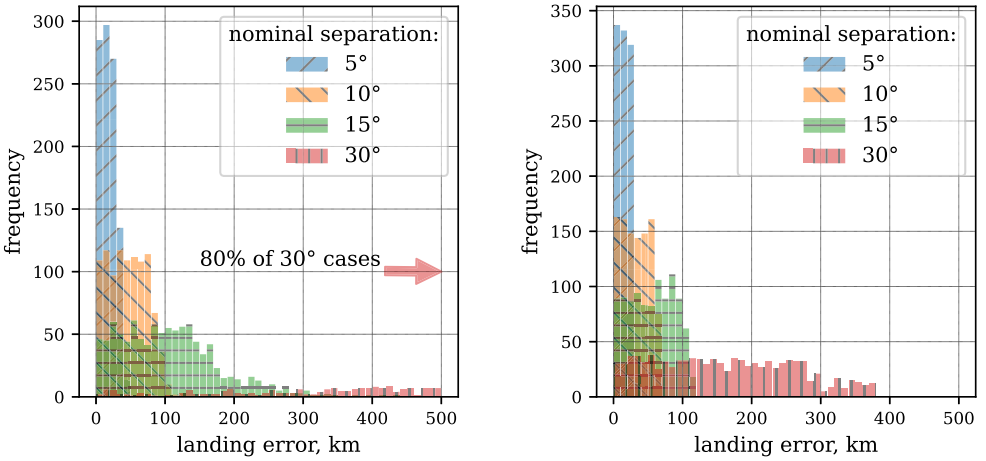

a) Downrange separations **b) Crossrange separations**

Fig. 14 Monte Carlo results for large-scale network.

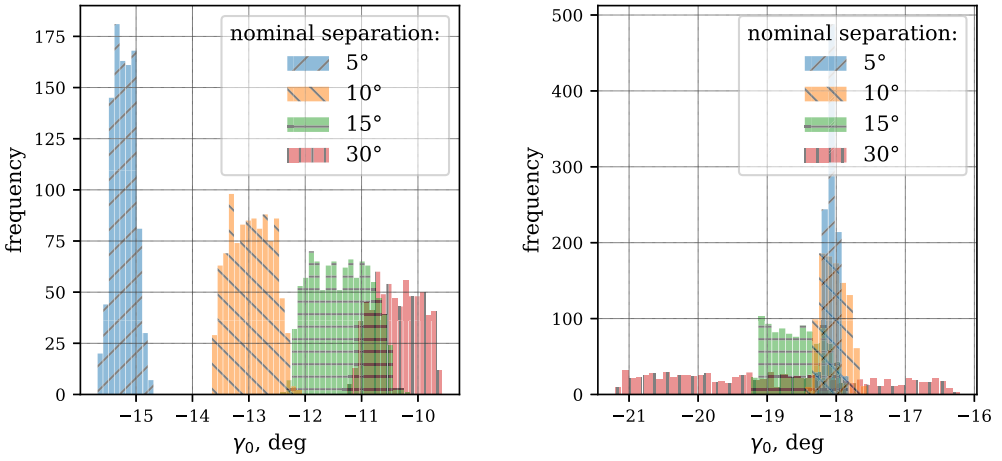

a) Downrange separation **b) Crossrange separation**

Fig. 15 Actual entry flight-path angles for probe trajectories.

the carrier 18 days before entry; the earlier separation time is selected to reduce the jettison speeds required to reach crossrange separations. The resulting nominal γ_0 values are, in order of increasing separation, −15.15, −12.79, −11.27, and −9.91 deg for the downrange separations and −17.82, −17.92, −18.54, and −19.04 deg for the crossrange separations. Figure 14 shows the resulting landing error for these eight probes, and Fig. 15 shows the resulting dispersed γ_0 values. It should be reiterated that γ_0 of the central approach trajectory, which is the same for all cases, is distinct from the actual flight-path angle of each probe upon entering the atmosphere.

From Fig. 14a, it is clear that landing error increases substantially with each increase in nominal downrange separation. The landing dispersions for the 10 and 15 deg cases are large but bounded, such that they would conceivably still suffice if the probes were targeting a broad region on the surface. In contrast, the 30 deg case has such a large landing error that 80% of the trials have greater than 500 km error; in 31% of the trials, the spacecraft skips out of the atmosphere while still on a hyperbolic trajectory. This large jump in error statistics is the result of the plateau in required jettison speed observed in Fig. 11a. Because very small changes in jettison speed result in huge changes in landing separation, the ±10% jettison speed dispersion is sufficient to radically degrade targeting. Clearly, under the assumed scenario and dispersions, the 30 deg downrange separation is not a viable trajectory, nor are the trajectories with greater downrange separation.

To get a sense of to what extent the error results from jettison speed dispersions, Fig. 16 shows the results of an equivalent Monte Carlo analysis but without jettison speed dispersions. All probe trajectories show marked improvement, including the 30 deg case, and no trajectories remain hyperbolic. However, the 30 deg case still has dramatically greater landing error than the other three cases, with the large majority of trials exceeding 100 km of error and 31% of the trials exceeding 500 km of error. This is because the extended coast phase, as seen in Fig. 12, results in a trajectory that is fundamentally more sensitive to variations. That is, even when perfect probe jettison execution is assumed, small variations have a major impact due to the shallow entry flight-path angle and close proximity to other trajectories in the solution family that extend much further in downrange.

Turning to crossrange separations, the landing error with dispersed jettison speed also increases substantially as desired separation increases, with the 30 deg case again performing much worse than the other three probes, but this time without any errors exceeding 500 km. However, in contrast to the downrange cases, the landing error results for the Monte Carlo analysis without jettison speed dispersions are relatively small and seemingly insensitive to the desired separation. The differing behavior comes down to the nominal entry flight-path angle for each probe. As desired downrange separation increases, the nominal γ_0 becomes shallower[§§] and, as shown in Fig. 15a, the variation in γ_0 increases. In contrast, the cross-range trajectories all have a nominal γ_0 near −18 deg, which is similar to the central approach trajectory, but the dispersions on γ_0 still increase with desired separation, as seen in Fig. 15b. As desired separation increases, so does

[§§]Note, though, that this trend plateaus as separations greater than 30 deg are targeted because the differences in entry interface states for these trajectories are very small.

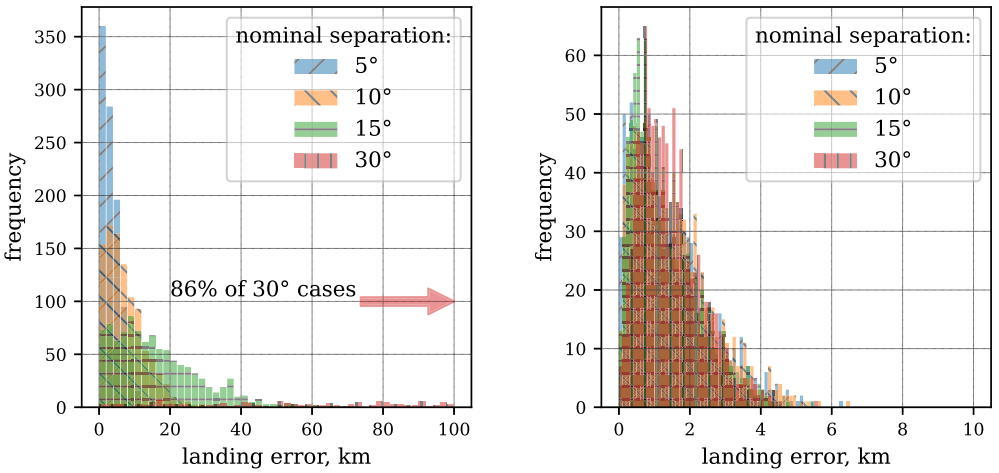

a) Downrange separations **b) Crossrange separations**

Fig. 16 Monte Carlo results for large-scale network without jettison speed dispersions.

required jettison speed, and thus the jettison speed dispersions have greater effect. Thus, when probe jettison execution error is removed from the assumed dispersions, all crossrange trajectories enter at about −18 deg and experience landing errors consistent with the single-probe flight-mechanics analysis shown in Fig. 5b. The larger γ_0 dispersions resulting from probe jettison execution error for the 30 deg crossrange case are what account for the much greater landing site dispersions seen in Fig. 14b; although this case is benign when compared to the largest downrange separation case, it still is most likely too much error for practical application.

VI. Conclusions

Networks of co-delivered probes on the Martian surface would be scientifically valuable at a range of scales, and this study examines some of the relevant flight-mechanics and mission design considerations. It is shown that regional networks within about 100 km of the central point can be co-delivered with a small mechanical jettison within five days of atmospheric entry. Larger networks are considered, and trajectories are successfully identified using numerical nonlinear optimization. However, the long coast and skip-out trajectories identified in this study are too sensitive to error to be practical beyond a certain separation distance, even under reduced targeting accuracy requirements. For the scenario considered here, this cutoff occurs beyond roughly 15 deg of desired separation, corresponding to a maximum separation of approximately 890 km along the surface in either direction. Several alternative approaches could potentially enable larger separations. For instance, the strict co-delivery assumption could be relaxed to allow the carrier spacecraft to perform multiple maneuvers during approach, including between separation events. Also, the probe jettisons could be performed much earlier, enabling different targeting geometries with much lower required jettison speeds as compared to similar geometries for separation within 20 days of entry. The targeting optimization process itself could be constrained to solutions with a desired entry flight-path angle, potentially resulting in larger probe jettison speeds but avoiding highly sensitive trajectories. An even more constrained approach would be to first define states at atmospheric entry interface that meet requirements and result in the desired landing locations, and then to design maneuvers targeting those entry states, effectively decoupling the exoatmospheric and atmospheric trajectory design processes. This decoupled approach would enable the desirable properties of the nominal atmospheric flight trajectories to be guaranteed, at the expense of potentially further increasing the required jettison speed.

Acknowledgments

This work was supported by a NASA Space Technology Research Fellowship. S. W. Albert gratefully acknowledges discussion with, and input and aerodynamic data provided by, the Small High Impact Energy Landing Device team at the Jet Propulsion Laboratory, including Louis Giersch, Nathan Barba, Ryan Woolley, and Chad Edwards. S. W. Albert also acknowledges ideas and advice from other participants in the Revolutionizing Access to the Martian Surface workshop organized by the W. M. Keck Institute for Space Studies, as well as at the Low-Cost Science Mission Concepts for Mars Exploration workshop. An earlier version of this work was presented as American Astronomical Society Paper 22-800 at the 2022 AAS/AIAA Astrodynamics Specialist Conference in Charlotte, North Carolina.

References

[1] Braun, R. D., and Manning, R. M., "Mars Exploration Entry, Descent, and Landing Challenges," *Journal of Spacecraft and Rockets*, Vol. 44, No. 2, 2007, pp. 310–323. https://doi.org/10.2514/1.25116

[2] Callahan, J., and Dreier, C., "Mars in Retrograde: A Pathway to Restoring NASA's Robotic Mars Exploration Program," Planetary Soc. TR, Pasadena, CA, 2017, http://planetary.s3.amazonaws.com/assets/pdfs/advocacy/2017/Mars-in-Retrograde-The-Planetary-Society-2017.pdf [retrieved 15 June 2023].

[3] Elfving, A., Elias, A. L., King, M. T., Lee, G., Pellicciotti, J., Theisinger, P. C., Thompson, D. W., Wadhwa, M., Young, T., and Zuber, M., "Mars Sample Return (MSR) Program: Final Report of the Independent Review Board (IRB)," NASA TR 201029b, 2020, https://www.nasa.gov/sites/default/files/atoms/files/nasa_esa_mars_sample_return_final_report_small.pdf [retrieved 15 June 2023].

[4] Culbert, C. J., Ehlmann, B. L., and Fraemen, A. A., "Revolutionizing Access to the Martian Surface," W. M. Keck Inst. for Space Studies Final Workshop Rept., Pasadena, CA, 2022, https://authors.library.caltech.edu/113539/2/Access2Mars-Final_Report-2022.pdf [retrieved 15 June 2023].

[5] Low-Cost Science Mission Concepts for Mars Exploration Workshop Science Organizing Committee, *Low-Cost Science Mission Concepts for Mars Exploration Final Report*, Jet Propulsion Lab., JPL D-109705, Pasadena, CA, 2022, https://www.hou.usra.edu/meetings/lowcostmars2022/ [retrieved 15 June 2023].

[6] Banfield, D., "Mars Science Goals, Objectives, Investigations, and Priorities: 2020 Version," Mars Exploration Program Analysis Group TR, Pasadena, CA, 2020, https://mepag.jpl.nasa.gov/reports/MEPAGGoals_2020_MainText_Final.pdf [retrieved 15 Sept. 2022].

[7] Diniega, S., Barba, N., Giersch, L., Jackson, B., Soto, A., Rafkin, S., Swann, C., Sullivan, R., Banfield, D., and Fenton, L., "Optimally-Sized Mission Concepts for Focused In-Situ Studies of Planetary Surface-Atmosphere Interactions," *Low-Cost Science Mission Concepts for Mars Workshop*, Jet Propulsion Lab., 2022, Paper 5044, https://www.hou.usra.edu/meetings/lowcostmars2022/pdf/5024.pdf [retrieved 15 June 2023].

[8] Stähler, S. C., Panning, M. P., Antonangeli, D., Banerdt, W. B., Banfield, D., Banks, M., Ceylan, S., Charalambous, C., Clinton, J., Daubar, I., Fernando, B., Giardini, D., Grott, M., Horleston, A., Hurst, K., Kawamura, T., Kim, D., Knapmeyer, M., Lorenz, R., Margerin, L., Marusiak, A., Menina, S., Mittelholz, A., Murdoch, N., Perrin, C., Pike, W. T., Schmelzbach, C., Schmerr, N., Schimmel, M., Spiga, A., Stott, A.,

Taylor, J., and Weber, R., "A Cerberus Fossae Seismic Network," *Low-Cost Science Mission Concepts for Mars Workshop*, Jet Propulsion Lab., 2022, Paper 5024, https://www.hou.usra.edu/meetings/lowcostmars2022/pdf/5024.pdf [retrieved 15 June 2023].

[9] Rafkin, S., "The Atmospheric Characterization for Exploration and Science (ACES) Instrument Suite for Mars," *2015 IEEE Aerospace Conference*, IEEE, New York, 2015, pp. 1–6. https://doi.org/10.1109/AERO.2015.7119061

[10] Nunn, C., Pike, W. T., Standley, I. M., Calcutt, S. B., Kedar, S., and Panning, M. P., "Standing on Apollo's Shoulders: A Microseismometer for the Moon," *Planetary Science Journal*, Vol. 2, No. 1, 2021, Paper 36.

[11] Scoon, G. E. N., and Whitcomb, G. P., "MARSNET: A Precursor to the Surface Exploration of Mars," *Acta Astronautica*, Vol. 29, No. 10, 1993, pp. 823–831. https://doi.org/10.1016/0094-5765(93)90164-R

[12] Squyres, S., "The Mars Environmental Survey (MESUR) Mission," *Advances in Space Research*, Vol. 15, No. 4, 1995, pp. 179–188. https://doi.org/10.1016/0273-1177(94)00079-G

[13] Harri, A.-M., Linkin, V., Polkko, J., Marov, M., Pommereau, J.-P., Lipatov, A., Siili, T., Manuilov, K., Lebedev, V., Lehto, A., Pellinen, R., Pirjola, R., Carpentier, T., Malique, C., Makarov, V., Khloustova, L., Esposito, L., Maki, J., Lawrence, G., and Lystsev, V., "Meteorological Observations on Martian Surface: Met-Packages of Mars-96 Small Stations and Penetrators," *Planetary and Space Science*, Vol. 46, No. 6, 1998, pp. 779–793. https://doi.org/10.1016/S0032-0633(98)00012-9

[14] Banderdt, B., Chicarro, A. F., Coradini, M., Federico, C., Greeley, R., Hechler, M., Knudsen, J. M., Leovy, C., Lognonne, P., Lowry, L., McCleese, D., McKay, C., Pellinen, R., Phillips, R., Scoon, G. E. N., Spohn, T., Squyres, S., Taylor, F., and Wanke, H., "INTERMARSNET: Phase-A Study Report," ESA Publ. D/SCI(96)2, Noordwijk, NL, April 1996.

[15] Smrekar, S., Catling, D., Lorenz, R., Magalhães, J., Moersch, J., Morgan, P., Murray, B., Presley, M., Yen, A., Zent, A., and Blaney, D., "Deep Space 2: The Mars Microprobe Mission," *Journal of Geophysical Research: Planets*, Vol. 104, No. E11, 1999, pp. 27,013–27,030. https://doi.org/10.1029/1999 JE001073

[16] Harri, A.-M., Marsal, O., Lognonne, P., Leppelmeier, G., Spohn, T., Glassmeier, K.-H., Angrilli, F., Banerdt, W., Barriot, J., Bertaux, J.-L., Berthelier, J., Calcutt, S., Cerisier, J., Crisp, D., Dehant, V., Giardini, D., Jaumann, R., Langevin, Y., Menvielle, M., Musmann, G., Pommereau, J., Di Pippo, S., Guerrier, D., Kumpulainen, K., Larsen, S., Mocquet, A., Polkko, J., Runavot, J., Schumacher, W., Siili, T., Simola, J., and Tillman, J., "Network Science Landers for Mars," *Advances in Space Research*, Vol. 23, No. 11, 1999, pp. 1915–1924. https://doi.org/10.1016/S0273-1177(99)00279-3

[17] Harri, A.-M., Pichkadze, K., Zeleny, L., Vazquez, L., Schmidt, W., Alexashkin, S., Korablev, O., Guerrero, H., Heilimo, J., Uspensky, M., Finchenko, V., Linkin, V., Arruego, I., Genzer, M., Lipatov, A., Polkko, J., Paton, M., Savijärvi, H., Haukka, H., Siili, T., Khovanskov, V., Ostesko, B., Poroshin, A., Diaz-Michelena, M., Siikonen, T., Palin, M., Vorontsov, V., Polyakov, A., Valero, F., Kemppinen, O., Leinonen, J., and Romero, P., "The MetNet Vehicle: A Lander to Deploy Environmental Stations for Local and Global Investigations of Mars," *Geoscientific Instrumentation, Methods and Data Systems*, Vol. 6, No. 1, 2017, pp. 103–124. https://doi.org/10.5194/gi-6-103-2017

[18] Barba, N., Komarek, T., Woolley, R., Giersch, L., Stamenković, V., Gallagher, M., and Edwards, C. D., "Mars Small Spacecraft Studies: Overview," *2019 IEEE Aerospace Conference*, IEEE, New York, 2019, pp. 1–10. https://doi.org/10.1109/AERO.2019.8741735

[19] Braun, R. D., Mitcheltree, R. A., and Cheatwood, F. M., "Mars Microprobe Entry-to-Impact Analysis," *Journal of Spacecraft and Rockets*, Vol. 36, No. 3, 1999, pp. 412–420. https://doi.org/10.2514/2.3461

[20] Edwards, C., and Matthies, L., "New Capabilities for Accessing the Martian Surface," Jet Propulsion Lab., California Inst. of Technology TR, Pasadena, CA, 2021, https://dataverse.jpl.nasa.gov/previewers/pdf_embed.html?fileid=73641&siteUrl=https://dataverse.jpl.nasa.gov [retrieved 15 June 2023].

[21] O'Neil, W. J., "The Galileo Spacecraft Architecture," *The Three Galileos: The Man, the Spacecraft, the Telescope*, Vol. 220, Springer, Dordrecht, The Netherlands, 1997, pp. 75–94.

[22] Kazeminejad, B., Atkinson, D. H., Pérez-Ayúcar, M., Lebreton, J.-P., and Sollazzo, C., "Huygens' Entry and Descent Through Titan's Atmosphere—Methodology and Results of the Trajectory Reconstruction," *Planetary and Space Science*, Vol. 55, No. 13, 2007, pp. 1845–1876. https://doi.org/10.1016/j.pss.2007.04.013

[23] Lo, M. W., Williams, B. G., Bollman, W. E., Han, D., Hahn, Y., Bell, J. L., Hirst, E. A., Corwin, R. A., Hong, P. E., Howell, K. C., Barden, B., and Wilson, R., "Genesis Mission Design," *Journal of the Astronautical Sciences*, Vol. 49, No. 1, 2001, pp. 169–184. https://doi.org/10.1007/BF03546342

[24] Desai, P. N., Lyons, D. T., Tooley, J., and Kangas, J., "Entry, Descent, and Landing Operations Analysis for the Stardust Entry Capsule," *Journal of Spacecraft and Rockets*, Vol. 45, No. 6, 2008, pp. 1262–1268. https://doi.org/10.2514/1.37090

[25] Yoshikawa, M., Kawaguchi, J., Fujiwara, A., and Tsuchiyama, A., "The Hayabusa Mission," *Sample Return Missions*, edited by A. Longobardo, Elsevier, New York, 2021, pp. 123–146. https://doi.org/10.1016/B978-0-12-818330-4.00006-9

[26] Tsuda, Y., Yoshikawa, M., Abe, M., Minamino, H., and Nakazawa, S., "System Design of the Hayabusa 2—Asteroid Sample Return Mission to 1999 JU3," *Acta Astronautica*, Vol. 91, Oct. 2013, pp. 356–362. https://doi.org/10.1016/j.actaastro.2013.06.028

[27] Williams, B., Antreasian, P., Carranza, E., Jackman, C., Leonard, J., Nelson, D., Page, B., Stanbridge, D., Wibben, D., Williams, K., Moreau, M., Berry, K., Getzandanner, K., Liounis, A., Mashiku, A., Highsmith, D., Sutter, B., and Lauretta, D. S., "OSIRIS-REx Flight Dynamics and Navigation Design," *Space Science Reviews*, Vol. 214, No. 4, 2018, Paper 69. https://doi.org/10.1007/s11214-018-0501-x

[28] Muirhead, B. K., Nicholas, A. K., Umland, J., Sutherland, O., and Vijendran, S., "Mars Sample Return Campaign Concept Status," *Acta Astronautica*, Vol. 176, Nov. 2020, pp. 131–138. https://doi.org/10.1016/j.actaastro.2020.06.026

[29] Garvin, J. B., Getty, S. A., Arney, G. N., Johnson, N. M., Kohler, E., Schwer, K. O., Sekerak, M., Bartels, A., Saylor, R. S., Elliott, V. E., Goodloe, C. S., Garrison, M. B., Cottini, V., Izenberg, N., Lorenz, R., Malespin, C. A., Ravine, M., Webster, C. R., Atkinson, D. H., Aslam, S., Atreya, S., Bos, B. J., Brinckerhoff, W. B., Campbell, B., Crisp, D., Filiberto, J. R., Forget, F., Gilmore, M., Gorius, N., Grinspoon, D., Hofmann, A. E., Kane, S. R., Kiefer, W., Lebonnois, S., Mahaffy, P. R., Pavlov, A., Trainer, M., Zahnle, K. J., and Zolotov, M., "Revealing the Mysteries of Venus: The DAVINCI Mission," *Planetary Science Journal*, Vol. 3, No. 5, 2022, Paper 117. https://doi.org/10.3847/PSJ/ac63c2

[30] Genova, A. L., Morrison-Fogel, D., Perez, A. D., and Cassell, A. M., "Trajectory Design for a Spacecraft Capable of Deploying Probes to the Martian Surface En Route to Low Mars Orbit," *2022 AAS/AIAA Astrodynamics Specialist Conference*, AAS Paper 22-729, 2022.

[31] Saikia, S. J., Rogers, B., Longuski, J. M., Saranathan, H., and Grant, M. J., "Strategies for Mars Network Science Missions via Innovative Aerocapture and EDL Architectures," *10th International Planetary Probe Workshop (IPPW-10)*, pp. 1–13, https://engineering.purdue.edu/~mjgrant/ippw10-paper-saikia-june.pdf [retrieved 15 June 2023].

[32] York, H. F., "Multiple-Warhead Missiles," *Scientific American*, Vol. 229, No. 5, 1973, pp. 18–27.

[33] Colin, L., "The Pioneer Venus Program," *Journal of Geophysical Research: Space Physics*, Vol. 85, No. A13, 1980, pp. 7575–7598. https://doi.org/10.1029/JA085iA13p07575

[34] Dorfman, S. D., and Meredith, C. M., "The Pioneer Venus Spacecraft Program," *Acta Astronautica*, Vol. 7, No. 6, 1980, pp. 773–795. https://doi.org/10.1016/0094-5765(80)90107-1

[35] Albert, S. W., Schaub, H., and Braun, R. D., "Flight Mechanics Feasibility Assessment for Co-Delivery of Direct-Entry Probe and Aerocapture Orbiter," *Journal of Spacecraft and Rockets*, Vol. 59, No. 1, 2022, pp. 19–32. https://doi.org/10.2514/1.A34953

[36] D'Amario, L. A., "Mars Exploration Rovers Navigation Results," *Journal of the Astronautical Sciences*, Vol. 54, No. 2, 2006, pp. 129–173. https://doi.org/10.1007/BF03256481

[37] Martin-Mur, T. J., Kruizinga, G. L., Burkhart, P. D., Abilleira, F., Wong, M. C., and Kangas, J. A., "Mars Science Laboratory Interplanetary Navigation," *Journal of Spacecraft and Rockets*, Vol. 51, No. 4, 2014, pp. 1014–1028. https://doi.org/10.2514/1.A32631

[38] Way, D., Powell, R., Chen, A., Steltzner, A., San Martin, M., Burkhart, P., and Mendeck, G., "Mars Science Laboratory: Entry, Descent, and Landing System Performance," *IEEE Aerospace Conference Proceedings*, IEEE Publ., Piscataway, NJ, 2006, pp. 1–19.

[39] Vinh, N. X., Busemann, A., and Culp, R. D., *Hypersonic and Planetary Entry Flight Mechanics*, Univ. of Michigan Press, Ann Arbor, MI, 1980, pp. 26–27, Chap. 2.

[40] Justh, H., "Mars Global Reference Atmospheric Model 2010 Version: Users Guide," NASA TM 2014-217499, 2014.

[41] Austin, A., Nelessen, A., Strauss, B., Ravich, J., Jesick, M., Venkatapathy, E., Beck, R., Wercinski, P., Aftosmis, M., Wilder, M., Allen, G., Braun, R., Werner, M., and Roelke, E., "SmallSat Aerocapture to Enable a New Paradigm of Planetary Missions," *2019 IEEE Aerospace Conference*, IEEE, New York, 2019, pp. 1–20. https://doi.org/10.1109/AERO.2019.8742220

[42] Vallado, D. A., *Fundamentals of Astrodynamics and Applications*, 4th ed., Microcosm Press, Portland, OR, 2013, pp. 1041–1042, Appendix D.

[43] Justus, C. G., and Braun, R. D., "Atmospheric Environments for Entry, Descent and Landing (EDL)," *5th International Planetary Probes Workshop and Short Course*, 2007, pp. 1–37, https://ntrs.nasa.gov/api/citations/20070032693/downloads/20070032693.pdf [retrieved 15 June 2023].

[44] Sutton, K., and Graves, R. A., "A General Stagnation-Point Convective-Heating Equation for Arbitrary Gas Mixtures," NASA TR R-376, 1971.

[45] Trainer, M. G., Wong, M. H., McConnochie, T. H., Franz, H. B., Atreya, S. K., Conrad, P. G., Lefèvre, F., Mahaffy, P. R., Malespin, C. A., Manning, H. L., Martín-Torres, J., Martínez, G. M., McKay, C. P., Navarro-González, R., Vicente-Retortillo, A., Webster, C. R., and Zorzano, M.-P., "Seasonal Variations in Atmospheric Composition as Measured in Gale Crater, Mars," *Journal of Geophysical Research: Planets*, Vol. 124, No. 11, 2019, pp. 3000–3024. https://doi.org/10.1029/2019 JE006175

[46] Way, D., "On the Use of a Range Trigger for the Mars Science Laboratory Entry, Descent, and Landing," *2011 Aerospace Conference*, IEEE, New York, 2011, pp. 1–8. https://doi.org/10.1109/AERO.2011.5747242

[47] Willcockson, W. H., "Mars Pathfinder Heatshield Design and Flight Experience," *Journal of Spacecraft and Rockets*, Vol. 36, No. 3, 1999, pp. 374–379. https://doi.org/10.2514/2.3456

[48] Putnam, Z. R., and Braun, R. D., "Precision Landing at Mars Using Discrete-Event Drag Modulation," *Journal of Spacecraft and Rockets*, Vol. 51, No. 1, 2014, pp. 128–138. https://doi.org/10.2514/1.A32633

[49] Fawley, D. M., and Putnam, Z. R., "Performance Assessment of Discrete-Event Drag Modulation for Mars Entry with Real-Time Guidance," *Journal of Spacecraft and Rockets*, Vol. 58, No. 4, 2021, pp. 1071–1083. https://doi.org/10.2514/1.A34796

[50] Albert, S. W., and Schaub, H., "Co-Delivery of Multiple Small Probes to the Martian Surface," *AIAA SciTech 2022 Forum*, AIAA Paper 2022-1653, 2022. https://doi.org/10.2514/6.2022-1653

[51] Giardini, D., Lognonné, P., Banerdt, W. B., Pike, W. T., Christensen, U., Ceylan, S., Clinton, J. F., van Driel, M., Stähler, S. C., Böse, M., Garcia, R. F., Khan, A., Panning, M., Perrin, C., Banfield, D., Beucler, E., Charalambous, C., Euchner, F., Horleston, A., Jacob, A., Kawamura, T., Kedar, S., Mainsant, G., Scholz, J.-R., Smrekar, S. E., Spiga, A., Agard, C., Antonangeli, D., Barkaoui, S., Barrett, E., Combes, P., Conejero, V., Daubar, I., Drilleau, M., Ferrier, C., Gabsi, T., Gudkova, T., Hurst, K., Karakostas, F., King, S., Knapmeyer, M., Knapmeyer-Endrun, B., Llorca-Cejudo, R., Lucas, A., Luno, L., Margerin, L., McClean, J. B., Mimoun, D., Murdoch, N., Nimmo, F., Nonon, M., Pardo, C., Rivoldini, A., Manfredi, J. A. R., Samuel, H., Schimmel, M., Stott, A. E., Stutzmann, E., Teanby, N., Warren, T., Weber, R. C., Wieczorek, M., and Yana, C., "The Seismicity of Mars," *Nature Geoscience*, Vol. 13, No. 3, 2020, pp. 205–212. https://doi.org/10.1038/s41561-020-0539-8

[52] Kedar, S., Panning, M. P., Smrekar, S. E., Stähler, S. C., King, S. D., Golombek, M. P., Manga, M., Julian, B. R., Shiro, B., Perrin, C., Power, J. A., Michaut, C., Ceylan, S., Giardini, D., Lognonné, P. H., and Banerdt, W. B., "Analyzing Low Frequency Seismic Events at Cerberus Fossae as Long Period Volcanic Quakes," *Journal of Geophysical Research: Planets*, Vol. 126, No. 4, 2021, Paper e2020 JE006518. https://doi.org/10.1029/2020 JE006518

[53] Lognonné, P., Banerdt, W. B., Giardini, D., Pike, W. T., Christensen, U., Laudet, P., de Raucourt, S., Zweifel, P., Calcutt, S., Bierwirth, M., Hurst, K. J., Ijpelaan, F., Umland, J. W., Llorca-Cejudo, R., Larson, S. A., Garcia, R. F., Kedar, S., Knapmeyer-Endrun, B., Mimoun, D., Mocquet, A., Panning, M. P., Weber, R. C., Sylvestre-Baron, A., Pont, G., Verdier, N., Kerjean, L., Facto, L. J., Gharakanian, V., Feldman, J. E., Hoffman, T. L., Klein, D. B., Klein, K., Onufer, N. P., Paredes-Garcia, J., Petkov, M. P., Willis, J. R., Smrekar, S. E., Drilleau, M., Gabsi, T., Nebut, T., Robert, O., Tillier, S., Moreau, C., Parise, M., Aveni, G., Ben Charef, S., Bennour, Y., Camus, T., Dandonneau, P. A., Desfoux, C., Lecomte, B., Pot, O., Revuz, P., Mance, D., tenPierick, J., Bowles, N. E., Charalambous, C., Delahunty, A. K., Hurley, J., Irshad, R., Liu, H., Mukherjee, A. G., Standley, I. M., Stott, A. E., Temple, J., Warren, T., Eberhardt, M., Kramer, A., Kühne, W., Miettinen, E.-P., Monecke, M., Aicardi, C., André, M., Baroukh, J., Borrien, A., Bouisset, A., Boutte, P., Brethomé, K., Brysbaert, C., Carlier, T., Deleuze, M., Desmarres, J. M., Dilhan, D., Doucet, C., Faye, D., Faye-Refalo, N., Gonzalez, R., Imbert, C., Larigauderie, C., Locatelli, E., Luno, L., Meyer, J.-R., Mialhe, F., Mouret, J. M., Nonon, M., Pahn, Y., Paillet, A., Pasquier, P., Perez, G., Perez, R., Perrin, L., Pouilloux, B., Rosak, A., Savin de Larclause, I., Sicre, J., Sodki, M., Toulemont, N., Vella, B., Yana, C., Alibay, F., Avalos, O. M., Balzer, M. A., Bhandari, P., Blanco, E., Bone, B. D., Bousman, J. C., Bruneau, P., Calef, F. J., Calvet, R. J., D'Agostino, S. A., de los Santos, G., , Deen, R. G., Denise, R. W., Ervin, J., Ferraro, N. W., Gengl, H. E., Grinblat, F., Hernandez, D., Hetzel, M., Johnson, M. E., Khachikyan, L., Lin, J. Y., Madzunkov, S. M., Marshall, S. L., Mikellides, I. G., Miller, E. A., Raff, W., Singer, J. E., Sunday, C. M., Villalvazo, J. F., Wallace, M. C., Banfield, D., Rodriguez-Manfredi, J. A., Russell, C. T., Trebi-Ollennu, A., Maki, J. N., Beucler, E., Böse, M., Bonjour, C., Berenguer, J. L., Ceylan, S., Clinton, J., Conejero, V., Daubar, I., Dehant, V., Delage, P., Euchner, F., Estève, I., Fayon, L., Ferraioli, L., Johnson, C. L., Gagnepain-Beyneix, J., Golombek, M., Khan, A., Kawamura, T., Kenda, B., Labrot, P., Murdoch, N., Pardo, C., Perrin, C., Pou, L., Sauron, A., Savoie, D., Stähler, S., Stutzmann, E., Teanby, N. A., Tromp, J., van Driel, M., Wieczorek, M., Widmer-Schnidrig, R., and Wookey, J., "SEIS: Insight's Seismic Experiment for Internal Structure of Mars," *Space Science Reviews*, Vol. 215, No. 1, 2019, Paper 12. https://doi.org/10.1007/s11214-018-0574-6

[54] Hopf, T., Kumar, S., Karl, W., and Pike, W., "Shock Protection of Penetrator-Based Instrumentation via a Sublimation Approach," *Advances in Space Research*, Vol. 45, No. 3, 2010, pp. 460–467. https://doi.org/10.1016/j.asr.2009.08.015

[55] Virtanen, P., Gommers, R., Oliphant, T. E., Haberland, M., Reddy, T., Cournapeau, D., Burovski, E., Peterson, P., Weckesser, W., Bright, J., van der Walt, S. J., Brett, M., Wilson, J., Millman, K. J., Mayorov, N., Nelson, A. R. J., Jones, E., Kern, R., Larson, E., Carey, C. J., Polat, İ., Feng, Y., Moore, E. W., VanderPlas, J., Laxalde, D., Perktold, J., Cimrman, R., Henriksen, I., Quintero, E. A., Harris, C. R., Archibald, A. M., Ribeiro, A. H., Pedregosa, F., and van Mulbregt, P., "SciPy 1.0: Fundamental Algorithms for Scientific Computing in Python," *Nature Methods*, Vol. 17, No. 3, 2020, pp. 261–272. https://doi.org/10.1038/s41592-019-0686-2

[56] Brent, R. P., *Algorithms for Minimization Without Derivatives*, Prentice–Hall, Englewood Cliffs, NJ, 1973, pp. 19–61, Chaps. 3–4.

[57] Nocedal, J., and Wright, S. J., *Numerical Optimization*, Springer, New York, 2006, pp. 136–143, Chap. 6.

D. P. Thunnissen
Associate Editor